Desalination 462 (2019) 48–55

Contents lists available at ScienceDirect

Desalination

journal homepage: www.elsevier.com/locate/desal

Response to comments on "comparison of energy consumption in desalination by capacitive deionization and reverse osmosis"

Mohan Qin[a,b,1], Akshay Deshmukh[a,b,1], Razi Epsztein[a,b], Sohum K. Patel[a,b], Oluwaseye M. Owoseni[b,c], W. Shane Walker[b,c], Menachem Elimelech[a,b,*]

[a] Department of Chemical and Environmental Engineering, Yale University, New Haven, CT 06520-8286, United States
[b] Nanosystems Engineering Research Center for Nanotechnology-Enabled Water Treatment (NEWT), Yale University, United States
[c] Department of Civil Engineering, The University of Texas at El Paso, W. University Ave., El Paso, TX 79968-0513, United States

1. Introduction

In our recently published article "Comparison of Energy Consumption in Desalination by Capacitive Deionization and Reverse Osmosis" [1], we proposed a simplified approach to model and compare the energetic performance of capacitive deionization (CDI) and reverse osmosis (RO). Based on specified operational conditions (i.e., feed salinity, water recovery, salt rejection, and average water flux), we showed that RO is significantly more energy efficient than CDI, particularly when targeting higher salinity feed streams and higher salt rejection values. In this Response, we address concerns and criticisms raised by Ramachandran et al. [2] regarding our proposed CDI model, strengthening the rigor and reliability of our results. We first clarify and discuss the underlying logic of using a Randles circuit to model CDI and validate the ohmic resistance values chosen for the two resistor elements in the circuit. It is important to note that our model aims to provide an effective tool to estimate the energetic performance of CDI desalination rather than a mechanistic description of the CDI process. Consequently, we do not seek to incorporate the electrochemical and electrokinetic phenomena involved mechanistically. We then clarify the energy efficiency and energy consumption trends obtained with our CDI model, emphasizing the merit of the Randles circuit model and the resistance values selected. We further reinforce the validity of our approach by comparing the energetic performance of CDI calculated using our Randles circuit model to a mechanistically-derived dynamic ion transport model. We conclude by using the dynamic ion transport model to confirm the results from our article, which showed that improvements in electrode materials yield only a marginal increase in energy efficiency.

2. Resistor elements in the Randles circuit

As Ramachandran et al. point out, the normalized resistance units used in the paper ($\Omega\,m^{-2}$) result in incorrect scaling of resistance with electrode area. Regrettably, in our original manuscript, we presented normalized resistance values in units of $\Omega\ m^{-2}$ by mistake. However, we have already issued a Corrigendum [3], correcting the normalized resistance values and presenting them in the correct units of $\Omega\ m^2$. Importantly, as we note in our Corrigendum, the normalization error only occurred in the text of our manuscript and did not propagate through any of the modeling calculations presented in our article. Hence, our results and conclusions remain unaffected. We refer the reader to our Corrigendum for further details regarding this unit error. Table 1 shows the area-normalized internal resistance and electrode resistance values with the correct units, as shown in Table 2 of our Corrigendum [3].

To predict the energetic performance of CDI over a wide range of operational conditions and to facilitate a comprehensive comparison with RO, we developed a readily tractable model based on a simplified Randles circuit rather than a mechanistically rigorous model (e.g., Helmholtz, Gouy-Chapman-Stern, and modified Donnan models). The Randles circuit is widely used as an equivalent circuit to model various complex electrochemical systems, including batteries, supercapacitors, and fuel cells [4–20]. Briefly, a Randles circuit is composed of a resistor (R_2) connected in parallel to a capacitor (C). The capacitor-resistor subunit is connected in series to another resistor element (R_1). A diagram of the circuit model is shown in Fig. 2 of our article [1]. Throughout the article, we use our Randles circuit model to capture the essential features of the energetic performance of CDI.

Ramachandran et al. suggest that the resistor R_2, which is connected in parallel to the capacitor, represents an unphysical short-circuiting of the capacitor. However, removing resistor R_2 assumes that all of the current driven by the power supply is used to charge the capacitor. This assumption is equivalent to assuming a charge efficiency of 100%, which, as previous literature has shown, is not reasonable in practical CDI systems [21–25]. In our Randles circuit model, resistor R_2 represents the non-idealities of electrical double layer (EDL) charging. The Randles circuit places resistor R_2 in parallel to the capacitor, which

* Corresponding author at: Department of Chemical and Environmental Engineering, Yale University, New Haven, CT 06520-8286, United States.
E-mail address: menachem.elimelech@yale.edu (M. Elimelech).
[1] These authors contributed equally to this work.

https://doi.org/10.1016/j.desal.2019.04.004
Received 1 April 2019; Accepted 1 April 2019
Available online 10 April 2019
0011-9164/

Table 1
Specified parameters for the CDI circuit model based on common values in CDI literature.

Parameter	Value
Capacitance, C ($F\,g^{-1}$)	60
Area-normalized internal resistance, $s\,A_e$ ($\Omega\,m^2$)	0.02
Area-normalized electrode resistance, $R_2\,A_e$ ($\Omega\,m^2$)	0.09

effectively leads to the applied external current (I_1 in Fig. 2 of our article) splitting between R_2 (I_2 in Fig. 2 of our article) and the capacitor (I_3 in Fig. 2 of our article). Therefore, in our model, R_2 represents all phenomena that do not constitute direct charging of the EDL in the electrodes. Ramachandran et al. claim that this leakage resistance should exclusively be attributed to Faradaic (parasitic) reactions. Throughout our study we intentionally maintained the potential below 1.5 V (as in typical CDI operation) to limit the presence of parasitic reactions (e.g., water splitting). Despite operation below the water splitting voltage, no experimental studies have achieved charge efficiencies of 100% [24,26–29]. Notably, charge efficiencies previously reported by the senior authors of this Comment vary between ~45% and 91% [23,30–33]. Losses in charge efficiency during low voltage operation are often attributed to co-ion repulsion or back-diffusion of counter-ions out of the electrode pores, ion swapping, and Faradaic reactions [34–40], all of which can be phenomenologically represented by R_2 in our model.

The basic assumptions of using the Randles circuit to represent a CDI stack comprising of multiple CDI cells are that (i) the CDI stack behaves as an electrical circuit in which all CDI cells are connected in parallel, (ii) each cell can be represented by a simplified Randles circuit, and (iii) the multi-cell CDI stack can be approximated as a single Randles circuit [41]. Recently, experimental current density and charge efficiency data from a commercial 17-cell CDI stack (Voltea B.V., the Netherlands) showed reliable fitting with the Randles circuit model [41], which reinforces the validity of the mentioned assumptions.

In their Comment, Ramachandran et al. criticize our use of the simplified Randles circuit model as a predictor of CDI energetic performance, claiming that impractical values of the resistances R_1 and R_2 "degrade performance". They further assert that an R_2/R_1 ratio on the order of 10^3 to 10^4, rather than the ratio used in our study (~10), is required to properly account for the amount of current that bypasses the capacitor. Fig. 1 shows the calculated charge efficiency (given by $\bar{I}_3/\bar{I}_1$, where $\bar{I}_1 = \int_0^{t_{charging}} I_1 dt$ and $\bar{I}_3 = \int_0^{t_{charging}} I_3 dt$) as a function of the resistance ratio R_2/R_1, ranging several orders of magnitude. The yellow shaded band represents the charge efficiencies of current CDI systems, which typically range from 65% to 96% [21,23–25,27–29,41]. From Fig. 1, it is clear that the R_2/R_1 ratios suggested by Ramachandran et al. are virtually equivalent to assuming that all applied current passes through the capacitor. This scenario assumes overestimated and impractical charge efficiency values ($\bar{I}_3/\bar{I}_1$) of nearly 100%.

Fig. 1 shows that the charge efficiency is most sensitive to R_2/R_1 ratio in the approximate region of one to ten (in which charge efficiency increases rapidly from 37% to 88%). An increase in the resistance ratio beyond a value of 100 yields a near 100% charge efficiency. The ratio of R_2/R_1 used in our article leads to a charge efficiency of 74%, resulting in a similar energy efficiency (3.1%) as calculated with fixed charge efficiency of 80% (3.6%). Furthermore, Owoseni [41] utilized least squares regression to fit values of C, R_1, and R_2 to data from CDI desalination experiments performed over a wide range of operational parameters. It was found that R_2/R_1 ratios were consistently within the same order of magnitude (~10), which is in direct agreement with our modeling.

Throughout our article [1], we assumed constant values of R_2 and charge efficiency. For future modeling, we note that the R_2 value can be adjusted as a function of charging/discharging time, flow efficiency,

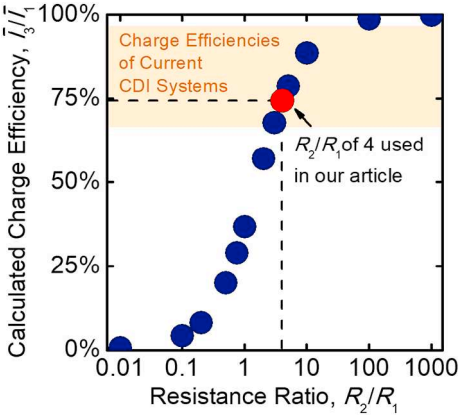

Fig. 1. Impact of resistance ratio (R_2/R_1) on the calculated charge efficiency ($\bar{I}_3/\bar{I}_1$). The area-normalized internal resistance ($s\,A_e$) is fixed at $0.02\,\Omega\,m^2$. $\bar{I}_1$ is the average applied current, while $\bar{I}_3$ represents the average current through the capacitor during the charging step. The blue circles represent the calculated charge efficiency ($\bar{I}_3/\bar{I}_1$), while the red circle shows the resistance ratio used in our article ($R_2/R_1 = 4$). The charging-step time is set at 300 s. The area-normalized electrode resistance ($R_2\,A_e$) is varied to achieve resistance ratios (R_2/R_1) from 0.01 to 1000. The yellow-shaded region represents the range of charge efficiencies typically reported in the literature [21,23–25,27–29,41]. (For interpretation of the references to color in this figure legend, the reader is referred to the web version of this article.)

cell voltage, and actual current losses (such as losses in EDL and Faradaic reactions). This modification would make the model more versatile and accurate in prediction of the charge efficiency. Nonetheless, our approach to utilize fixed R_2 and charge efficiency values is a tractable and effective way to capture the key features of CDI energetic performance.

The authors of the Comment also suggest that the values of R_1 utilized are "high" and further hinder the energetic performance of CDI. In our model, R_1 represents the sum of the fixed internal resistance (s) and the solution (ionic) resistance in the spacer channel which depends on the feed salinity and salt rejection (salinity of the product water). The internal resistance is composed of the ion-exchange membrane resistance, contact resistance between electrode and current collector, and ionic resistance in the electrodes (assumed to be constant). The area-normalized internal resistance was fixed at a constant value of $200\,\Omega\,cm^2$ throughout our modeling.

Similar in definition to our R_1, Qu et al. [42] characterized the area-normalized operational resistance (ANONR) as the sum of the contact, ionic (in spacer and electrodes), membrane, and current collector resistances. Therefore, it is sensible that our area-normalized R_1 values should be comparable to the ANONR values from experimental data. Through electrochemical impedance spectroscopy, Qu et al. determined an ANONR of $72.8\,\Omega\,cm^2$ for their custom-built single cell CDI stack. However, this value is considerably lower than the ANONR values determined from several other experimental studies which ranged from $160\,\Omega\,cm^2$ to $2517\,\Omega\,cm^2$ [42–49]. It is important to note that in Qu et al.'s review of cell resistances from previous work, only one other value is reported to be below $200\,\Omega\,cm^2$, with most resistances being well over $1000\,\Omega\,cm^2$. With respect to these published resistance values, the R_1 value utilized in our model is reasonably low and representative of a well-designed CDI cell.

3. Trends of thermodynamic energy efficiency and energy consumption by the Randles circuit model

Ramachandran et al. claim that the trends shown in Fig. 8A of our article [1] are "unphysical" because, in certain regions, the energy efficiency decreases with increasing water recovery. In Fig. 8A of our article, a wide range of water recovery ratios and salt rejection values

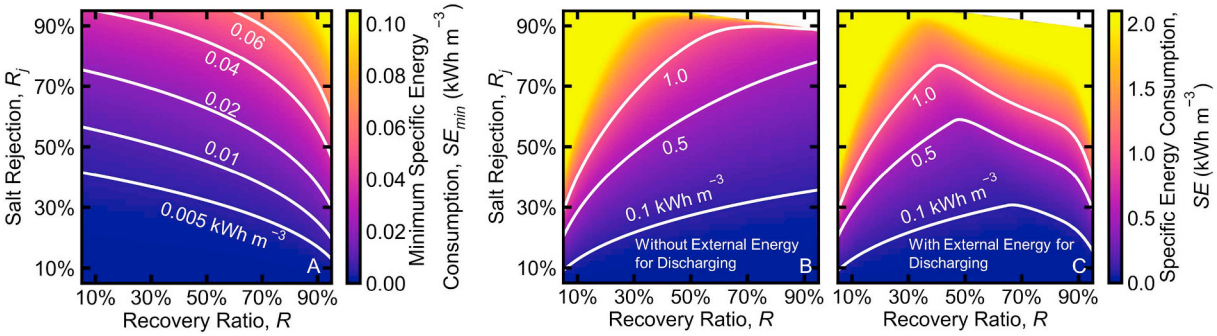

Fig. 2. (A) The theoretical minimum specific energy consumption (SE_{min}), (B) specific energy consumption (SE) without external energy for discharging step, and (C) SE with external energy for discharging as a function of water recovery ratio (R) and salt rejection (R_j). The SE_{min} is defined as the specific energy consumption of a thermodynamically reversible process operating with the same feed, brine, and product streams. Specific SE_{min} and SE values are indicated using an overlaid contour map (white curves). The feed salt concentration and average water flux are fixed at 2 g L^{-1} and 10 L m^{-2} h^{-1}, respectively, throughout. The charging-step time is fixed at 300 s, while discharging time varies from 6000 s (5% water recovery) to 15 s (95% water recovery). The charging and discharging steps have the same flow rate. In (B), no external energy is applied during discharging step. In (C), an external reverse current is applied during the discharging step when required to release salt ions prior to the next charging step. The required reverse current varies according to the water recovery ratio and salt rejection. The water recovery and salt rejection values in the blank region at the top right cannot be achieved for the specified average water flux and charging-step time.

are achieved by varying the applied current, discharging-step time, and charging and discharging flowrates. The feed salt concentration is fixed at 2 g L^{-1}, throughout. We use equal flowrate for charging and discharging steps, which is the typical operational mode for CDI [28,33,49–53]. The charging-step time is fixed at 300 s, while the discharging-step time is varied to alter the water recovery. Subsequently, the flowrate is varied to achieve the fixed average water flux of 10 L m^{-2} h^{-1}. Energy recovery is not included in Fig. 8A as it is considered later in Fig. 9 of our article.

Fig. 2A illustrates how the theoretical minimum specific energy consumption (SE_{min}) (Eq. (14) in our article) increases with water recovery ratio (R) and salt rejection (R_j). We also show the trend of specific energy consumption (SE) as a function of water recovery and salt rejection in two cases—without external energy input during the discharging step (Fig. 2B) and with external energy input during the discharging step (Fig. 2C). When no external energy is applied during the discharging step, increasing the water recovery ratio leads to a decrease in SE (Fig. 2B). For a fixed salt rejection and average water flux, increasing the water recovery necessitates reducing the discharging-step time; thus, the total cycle time is also decreased. To achieve the same average water flux, less product water (volume) would have to be generated during the charging step, and hence less total salt would be removed. Therefore, lower applied current would be required, which ultimately results in a lower SE. For example, to achieve a salt rejection of 50% and 10 L m^{-2} h^{-1} average water flux, increasing the water recovery from 30% to 70% leads to a 53% reduction in SE from 0.54 kWh m^{-3} to 0.25 kWh m^{-3}.

Overall, in the absence of external energy input for discharging, the energy efficiency increases monotonically with increasing water recovery (Fig. A1 in the Appendix), resulting from a decrease in SE and an increase in SE_{min}. However, particular regions of high water recovery and salt rejection require especially short discharging-step times. In these cases, an external reverse current must be applied to facilitate the rapid rates of salt desorption needed for regeneration of the electrodes. Without the application of a reverse current, the relatively slow desorption of ions from the electrodes limits the water recovery and results in salt accumulation in the electrodes, leading to progressive deterioration in capacitance and performance with repeated charging-discharging cycles. An external reverse current is commonly used in practical CDI systems to ensure that complete electrode discharge is achieved [38,49,54,55].

The application of external energy input for salt desorption leads to a high energy consumption (Fig. 2C) and a low energy efficiency (Fig. 8A of our article) at high water recovery values. For example, at 70% water recovery and 70% salt rejection, the reverse current input during the discharging step increases the SE from 0.50 kWh m^{-3} to 1.4 kWh m^{-3}, corresponding to a decrease in energy efficiency from 6.9% to 2.6%. Fig. A2 (in the Appendix) shows the same trend for CDI energy efficiency as a function of water recovery and salt rejection ratios for lower area-normalized internal resistances (s A_e) of 0.01 Ω m^2 and 0.005 Ω m^2. In each case, decreasing salt rejection leads to an increase in energy efficiency. This demonstrates that a lower R_1 value will not change the trend observed in our article, which is in contrast to the claim by Ramachandran et al. In the Comment, Ramachandran et al. assume 100% energy recovery and do not account for the external energy input required to achieve high water recovery ratios.

4. Comparison of energetic performance calculated using the Randles circuit with a dynamic ion transport model

We employed a mechanistic dynamic ion transport model to compare the energetic performance of CDI with our Randles circuit model. The dynamic ion transport model relies on modified Donnan (mD) theory to describe the EDL structure within the porous carbon electrodes, and it is a commonly utilized model to simulate CDI performance [27,50,56–61]. The porous carbon material is assumed to consist of macropores, which allow for ion transport throughout the electrode, and micropores, where EDL is formed [57–59]. Charge neutrality is assumed in the macropores, while the EDL structure in the micropores predominantly contributes to the ion adsorption capacity. The key governing equations of the model are described in the Appendix, and further assumptions and details about the transport theory can be found in previous literature [27,50,56,58,60,61]. The values of the parameters used in the model are summarized in Table A1 of the Appendix.

Fig. 3 shows the data presented in Figs. 6A and 7A in our article with the corresponding results from the dynamic ion transport model overlaid. The specific energy consumptions (SE) calculated using both models for feed salinities of 1 g L^{-1} and 2 g L^{-1} are shown as a function of salt rejection in Fig. 3A. In these calculations, the water recovery ratio, average water flux, and charging-step time are fixed at 50%, 10 L m^{-2} h^{-1}, and 100 s, respectively. Fig. 3A reveals that the same trend is observed with both models—a higher salt rejection requires a higher current input, resulting in a greater SE. The SE calculated by the dynamic ion transport model is slightly higher than that calculated by the Randles circuit model. We also compare the SE calculated using our Randles circuit model with corresponding values from a very recent study by the senior authors of the Comment and other leading CDI researchers [23]. Notably, our Randles circuit model is able to replicate

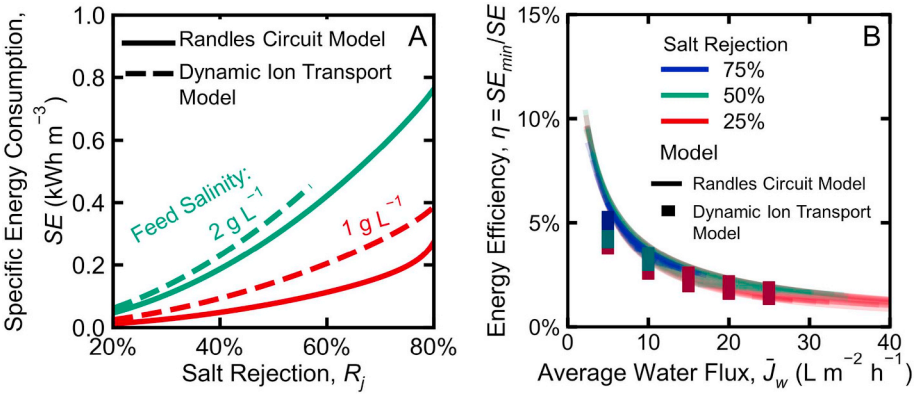

Fig. 3. Comparison of the specific energy consumption and energy efficiency obtained from the Randles circuit model and the mechanistic dynamic ion transport model. (A) Specific energy consumption as a function of salt rejection for feed salinities of 1 g L^{-1} and 2 g L^{-1}. The solid curves are calculated using the Randles circuit model, whereas the dashed curves are calculated using the dynamic ion transport model. The average water flux (normalized by projected electrode area) is fixed at 10 L m^{-2} h^{-1}. Both the charging- and discharging-step times are fixed at 100 s. Water recovery is fixed at 50% for all calculations. Different salt rejections are achieved by varying the applied current. (B) Energy efficiency as a function of average water flux for salt rejection values of 25%, 50%, and 75%. Solid curves are calculated using the Randles circuit model, while symbols (cubes) represent values calculated using dynamic ion transport model. The water recovery ratio and feed salt concentration are fixed at 50% and 2 g L^{-1}, respectively. The charging-step time, which is the same as discharging-step time for 50% water recovery, varied from 400 s to 100 s. For both (A) and (B), the values of parameters used in the dynamic ion transport model are presented in Table A1 of the Appendix.

the trends illustrated in Fig. 2B of their article [23], namely *SE* increases linearly with increasing average water flux at a fixed salt rejection. In fact, the *SE* values that our model predicts are lower than their calculations, which assume 100% energy recovery, particularly for high salt rejection values. For example, for a feed salinity of 2.9 g L^{-1} (50 mM) and a salt rejection of 30%, the *SE* calculated using our Randles circuit model is 1.3 kWh m^{-3}, while the authors of the Comment show a corresponding *SE* of 2.0 kWh m^{-3} in Fig. 2B of their article [23]. Consequently, we do not believe that our Randles circuit model underestimates the energetic performance of CDI desalination as the Comment suggests.

The trade-off between energy efficiency and average water flux is also shown with the dynamic ion transport model for salt rejection values of 25%, 50%, and 75% (Fig. 3B). The energy efficiency calculated from the dynamic ion transport model is comparable to the data in Fig. 7A of our article. For each salt rejection, increasing the average water flux leads to a rapid decrease in energy efficiency. Fig. A3 in the Appendix, which shows energy efficiency as a function of water recovery and salt rejection, further highlights the agreement in trends between the Randles circuit and dynamic ion transport models. Overall, the consistency in trends among the two models indicates that the simplified Randles circuit is capable of simulating key aspects of the energetic performance of CDI. Additionally, the energy efficiency values calculated using our model and reported in our article are comparable to the energy efficiencies observed in previous experimental studies, which are summarized in Tables S1 and S2 of a recently published review [56].

In our article, we showed that further improvements in electrode materials have a limited potential for enhancing the energy efficiency of CDI (Fig. 9A in our article). In contrast, Ramachandran et al. assert in their Comment that increasing capacitance can significantly improve the energy efficiency. To confirm the validity of our findings, we compared our Randles circuit model results with the dynamic ion transport model. In Fig. 4, we show the energy efficiency calculated with the dynamic ion transport model as a function of average water flux for a wide range of electrode capacitance values. Clearly, the data from the dynamic ion transport model reveals the same diminishing effect on energy efficiency with increasing electrode capacitance. In addition, the results presented in Fig. 4 reinforce the trends we observed using the Randles circuit model, and furthermore reveal that mechanistic modeling predicts even more severe limitations on CDI energy efficiency than the Randles circuit model. For example, increasing electrode capacitance from the typical value of activated carbon electrodes (60 F g^{-1}) to an ultra-high value of 1000 F g^{-1} at 5 L m^{-2} h^{-1} leads to only ~25% improvement in the energy efficiency (from 4% to 5%). This value is half the ~50% improvement predicted by the Randles circuit model under the same conditions (which showed an increase in energy efficiency from 5% to 10%).

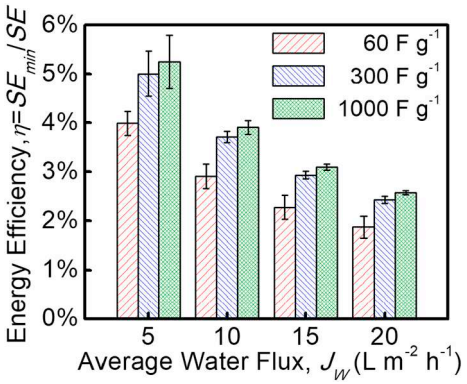

Fig. 4. Energy efficiency of CDI calculated using the mechanistic dynamic ion transport model with electrode capacitance of 60, 300, and 1000 F g^{-1}. The average water fluxes are 5, 10, 15, and 20 L m^{-2} h^{-1}. The feed salt concentration and salt rejection are fixed at 2 g L^{-1} and 25%, respectively. The charging-step time, which is the same as discharging-step time for 50% water recovery, varied from 400 s to 100 s. The error bars reflect the variation of energy efficiency caused by the different charging-step times. For salt rejection of 25%, the applied current is varied according to the charging-step time, resulting in a range of energy efficiency values. The average water flux is defined as the volume of product water during the charging step divided by the total electrode surface area and the total charging and discharging times. The values of parameters used in the dynamic ion transport model are presented in Table A1 of the Appendix.

5. Concluding remarks

We have demonstrated that the relatively simple Randles circuit model is adequate for estimating the energetic performance of CDI. The predictions and trends in energy consumption derived using our circuit model are comparable to those obtained using the mechanistic and more complex dynamic ion transport model. The strong agreement between these CDI models in estimating energy consumption further supports our analysis and main conclusions in the article. Specifically, the two main conclusions are: (i) the energy efficiency of CDI is significantly lower than that of RO for brackish water desalination and (ii) improvements of electrode materials will have a limited impact on the energy efficiency of CDI.

Our article has shown that for a limited range of conditions—very low salt rejection (< ~25%) and low average water flux (< ~10 L m^{-2} h^{-1})—the energy efficiency of CDI is slightly greater than RO. However, the energy consumption in this case is extremely low (< ~0.02 kWh m^{-3}) and thus energy efficiency is not of practical

significance. Furthermore, desalination applications requiring such low salt rejection are rather limited, and in the few cases that such applications are needed, a more holistic approach should be implemented when selecting a desalination process. Other important factors that should be considered include capital and operating costs, operation at high water recovery to minimize the volume of concentrate waste streams, meeting multiple water quality objectives by simultaneous removal of a wide range of contaminants (e.g., uncharged solutes and natural organic matter), performance deterioration due to fouling and inorganic scaling, and reliability and ease of operation. Our discussion in the article suggests that RO outperforms CDI in several of these factors, most notably capital cost and removal of uncharged contaminants.

Acknowledgements

This work was supported by the NSF Nanosystems Engineering Research Center for Nanotechnology-Enabled Water Treatment (EEC-1449500).

Appendix A. Dynamic ion transport model

This section details the key equations used in the dynamic ion transport model. Details about the theory and governing equations can be found in previous literature [27,50,56,58,60,61].

The ion concentration inside the micropores is calculated as

$$c_{i,mi} = c_{mA}\exp(-z_i\Delta\phi_d) \tag{A1}$$

where $c_{i,mi}$ is the concentration of ion i in the micropores, c_{mA} is the salt concentration in the macropores, z_i is the ion charge (for monovalent salt, $+1$ for the cation and -1 for the anion), and $\Delta\phi_d$ is the dimensionless Donnan potential difference between the micropores and the macropores (e.g. $\Delta\phi_d$ multiplied by the thermal voltage, V_T, gives units of volts).

The charge density inside the micropores (σ_{mi}) is the difference between $c_{cation,mi}$ and $c_{anion,mi}$, and is related to the potential drop across the Stern layer:

$$\sigma_{mi} = c_{cation,mi} - c_{anion,mi} = -2c_{mA}\sinh(\Delta\phi_d) \tag{A2}$$

$$\sigma_{mi}F = -C_{st,vol}\Delta\phi_{st}V_T \tag{A3}$$

where F is the Faraday constant, $\Delta\phi_{st}$ is the Stern layer potential, and $C_{st,vol}$ is the volumetric Stern layer capacitance.

During the charging step, both the volumetric charge density and the ion concentrations in the electrode micro- and macropores change with respect to time:

$$\frac{\partial}{\partial t}(p_{mi}\sigma_{mi}) = \frac{I}{L_{elec}F} \tag{A4}$$

$$\frac{\partial}{\partial t}(2p_{mA}c_{mA} + p_{mi}c_{mi,ions}) = \frac{J_{ions}}{L_{elec}} \tag{A5}$$

where p_{mA} is the macropore porosity, p_{mi} is the micropore porosity, L_{elec} is the electrode thickness, I is the applied current, $c_{mi,ions}$ is the micropore ion concentration, and J_{ions} is the ion flux.

In the spacer channel, the variation of salt concentration (c_{sp}) with time is calculated by:

$$\frac{\partial c_{sp}}{\partial t} = -\frac{J_{ions}}{L_{sp}} + \frac{c_{sp,inflow} - c_{sp}}{\tau} \tag{A6}$$

where c_{sp} is the salt concentration in the spacer, L_{sp} is the spacer thickness, $c_{sp,inflow}$ is the influent concentration, and τ is the hydraulic retention time in the spacer channel.

The current density depends on the electrical potential difference across the spacer channel and the spacer salt concentration:

$$I = -4c_{sp}DF\frac{\Delta\phi_{sp,half}}{L_{sp}} \tag{A7}$$

where D is the diffusion coefficient of ions in the bulk solution, $\Delta\phi_{sp,half}$ is half of the spacer channel potential drop, and L_{sp} is the spacer thickness.

The potential drop in the electrode is related to the salt concentration in the macropores and the current density according to:

$$\Delta\phi_{elec}V_T = IR_{elec}/c_{mA} \tag{A7}$$

where R_{elec} is the specific electrode resistance.

The current density in the ion exchange membranes (IEMs) is calculated by:

$$I = -\bar{c}_{mem}D_{mem}F\frac{\Delta\phi_{mem}}{L_{mem}} \tag{A8}$$

where D_{mem} is the diffusion coefficient of the ions in the membrane, $\bar{c}_{mem}$ is the average ion concentration in the membrane, and L_{mem} is the membrane thickness. Approximately, $\bar{c}_{mem}$ is calculated as the average of the ion concentrations at the two interfaces (i.e. membrane/spacer $c_{mem/sp}$, and membrane/electrode $c_{mem/elec}$), which are given by the following equations:

$$c_{mem/elec} = 2c_{mA}\cosh(\Delta\phi_{m/e}) \tag{A9}$$

$$c_{mem/sp} = 2c_{sp}\cosh(\Delta\phi_{m/sp}) \tag{A10}$$

$$\bar{c}_{mem} = \frac{c_{mem/elec} + c_{mem/sp}}{2} \tag{A11}$$

The Donnan potentials at the two interfaces are:

$$\Delta\phi_{mem/sp} = \text{arcsinh}\left(\frac{\omega X}{c_{sp}}\right) \tag{A12}$$

$$\Delta\phi_{mem/elec} = \text{arcsinh}\left(\frac{\omega X}{c_{mA}}\right) \tag{A13}$$

where ω is the sign of the membrane charge (+1 for anion exchange membranes, and −1 for cation exchange membranes), and X is the intrinsic membrane charge density.

The ion flux (J_{ions}) can be expressed as

$$J_{ions} = -\frac{D_{mem}}{L_{mem}}(\Delta c_{mem} - \omega X \Delta\phi_{mem}) \tag{A14}$$

where Δc_{mem} is the difference between the ion concentrations at the two membrane interfaces.

Lastly, the cell voltage is calculated according to the sum of the potential drops (including the potential drop in external resistance R_{ext}), while the specific energy consumption is calculated based on the voltage and current as shown in our article.

Table A1
Parameters used in the dynamic ion transport model [1,27,50,56,58,60,61].

Symbols	Description	Value	Dimension
α	Charge dependence coefficient of Stern capacitance	20	F m^3 mol^{-2}
p_{ma}	Electrode macroporosity	0.40	
p_{mi}	Electrode microporosity	0.28	
$C_{st,vol,0}$	Volumetric Stern layer capacitance at zero charge	168	F mL^{-1}
L_{elec}	Electrode thickness	280	μm
L_m	Ion exchange membrane thickness	150	μm
L_{sp}	Spacer thickness	100	μm
D	Diffusion coefficient in bulk solution	1.68×10^{-5}	cm^2 s^{-1}
D_{mem}	Diffusion coefficient in the membrane	1.12×10^{-5}	cm^2 s^{-1}
$R_{electrode}$	Specific electrode resistance	0.6	Ω mol m^{-1}
R_{ext}	External resistance	40	Ω cm^2
X	Charge density of ion exchange membrane	5	mol L^{-1}

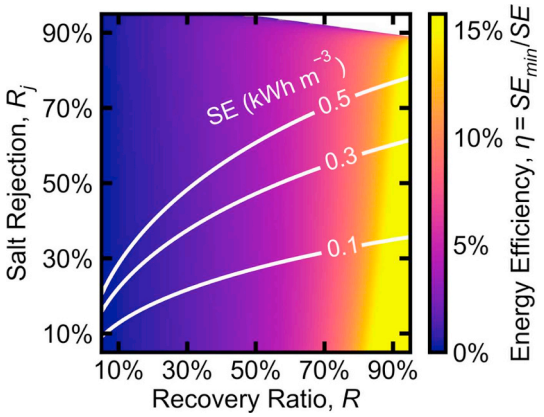

Fig. A1. Color map of the energy efficiency (η) as a function of water recovery ratio (R) and salt rejection (R_j) for CDI without external energy input during discharging step. Energy efficiency is defined as the thermodynamic minimum specific energy consumption divided by the specific energy consumption (SE). Specific energy consumption (SE) values are indicated using an overlaid contour map (white curves). The feed salt concentration and average water flux are fixed at 2 g L^{-1} and 10 L m^{-2} h^{-1}, respectively, throughout. The charging-step time is fixed at 300 s, while discharging time varies from 6000 s (5% water recovery) to 15 s (95% water recovery). The charging and discharging steps have the same flow rate. When required, an external reverse current is applied during the discharging step to release salt ions prior to the next charging step. The required reverse current varies according to the water recovery ratio and salt rejection. The water recovery and salt rejection values in the blank region at the top right cannot currently be achieved for the specified average water flux and charging-step time.

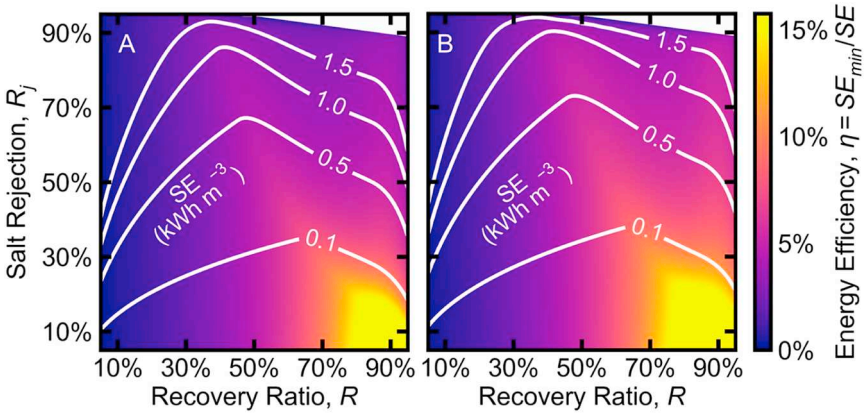

Fig. A2. Color maps of the energy efficiency (η) as a function of water recovery ratio (R) and salt rejection (R_j) for CDI with area-normalized internal resistances, $s\,A_e$, of (A) 0.01 Ω m^2 and (B) 0.005 Ω m^2. Specific energy consumption (SE) values are indicated using an overlaid contour map (white curves). The feed salt concentration and average water flux are fixed at 2 g L^{-1} and 10 L m^{-2} h^{-1}, respectively, throughout. The charging-step time is fixed at 300 s, while discharging time varies from 6000 s (5% water recovery) to 15 s (95% water recovery). The charging and discharging steps have the same flow rate. When required, an external reverse current is applied during the discharging step to release salt ions prior to the next charging step. The required reverse current varies according to the water recovery ratio and salt rejection. The water recovery and salt rejection values in the blank region at the top right cannot currently be achieved for the specified average water flux and charging-step time.

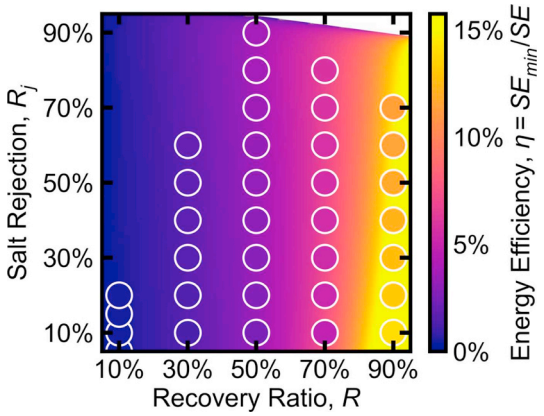

Fig. A3. Comparison of the energy efficiency calculated using the Randles circuit model and the dynamic ion transport model for CDI without external energy input during the discharging step. The color map is the same as in Fig. A1, while the colored circles represent the energy efficiency calculated using the dynamic ion transport model. The operation conditions are the same as in Fig. A1. The values of parameters used in the dynamic ion transport model are presented in Table A1.

References

[1] M. Qin, A. Deshmukh, R. Epsztein, S.K. Patel, O.M. Owoseni, W.S. Walker, M. Elimelech, Comparison of energy consumption in desalination by capacitive deionization and reverse osmosis, Desalination 455 (2019) 100–114.

[2] A. Ramachandran, D.I. Oyarzun, S.A. Hawks, P.G. Campbell, M. Stadermann, J.G. Santiago, Comments on "Comparison of energy consumption in desalination by capacitive deionization and reverse osmosis", Desalination 461 (2019) 30–36.

[3] M. Qin, A. Deshmukh, R. Epsztein, S.K. Patel, O.M. Owoseni, W.S. Walker, M. Elimelech, Corrigendum to "Comparison of energy consumption in desalination by capacitive deionization and reverse osmosis", Desalination 461 (2019) 55.

[4] B. Wang, S.E. Li, H. Peng, Z. Liu, Fractional-order modeling and parameter identification for lithium-ion batteries, J. Power Sources 293 (2015) 151–161.

[5] C. Masarapu, H.F. Zeng, K.H. Hung, B. Wei, Effect of temperature on the capacitance of carbon nanotube supercapacitors, ACS Nano 3 (2009) 2199–2206.

[6] A. Moya, Identification of characteristic time constants in the initial dynamic response of electric double layer capacitors from high-frequency electrochemical impedance, J. Power Sources 397 (2018) 124–133.

[7] S. Fiorenti, J. Guanetti, Y. Guezennec, S. Onori, Modeling and experimental validation of a hybridized energy storage system for automotive applications, J. Power Sources 241 (2013) 112–120.

[8] L. Zhang, Z. Wang, X. Hu, F. Sun, D.G. Dorrell, A comparative study of equivalent circuit models of ultracapacitors for electric vehicles, J. Power Sources 274 (2015) 899–906.

[9] S. Prabaharan, R. Vimala, Z. Zainal, Nanostructured mesoporous carbon as electrodes for supercapacitors, J. Power Sources 161 (2006) 730–736.

[10] S. Nejad, D. Gladwin, D. Stone, A systematic review of lumped-parameter equivalent circuit models for real-time estimation of lithium-ion battery states, J. Power Sources 316 (2016) 183–196.

[11] M. Jana, S. Saha, P. Khanra, P. Samanta, H. Koo, N.C. Murmu, T. Kuila, Non-covalent functionalization of reduced graphene oxide using sulfanilic acid azocromotrop and its application as a supercapacitor electrode material, J. Mater. Chem. A 3 (2015) 7323–7331.

[12] S. Hashmi, S. Suematsu, K. Naoi, All solid-state redox supercapacitors based on supramolecular 1, 5-diaminoanthraquinone oligomeric electrode and polymeric electrolytes, J. Power Sources 137 (2004) 145–151.

[13] S. Khamlich, Z. Abdullaeva, J. Kennedy, M. Maaza, High performance symmetric supercapacitor based on zinc hydroxychloride nanosheets and 3D graphene-nickel foam composite, Appl. Surf. Sci. 405 (2017) 329–336.

[14] N. Fouquet, C. Doulet, C. Nouillant, G. Dauphin-Tanguy, B. Ould-Bouamama, Model based PEM fuel cell state-of-health monitoring via ac impedance measurements, J. Power Sources 159 (2006) 905–913.

[15] B. Andreaus, A. McEvoy, G. Scherer, Analysis of performance losses in polymer electrolyte fuel cells at high current densities by impedance spectroscopy, Electrochim. Acta 47 (2002) 2223–2229.

[16] C. Brunetto, A. Moschetto, G. Tina, PEM fuel cell testing by electrochemical impedance spectroscopy, Electr. Power Syst. Res. 79 (2009) 17–26.

[17] Z. He, F. Mansfeld, Exploring the use of electrochemical impedance spectroscopy (EIS) in microbial fuel cell studies, Energy Environ. Sci. 2 (2009) 215–219.

[18] N. Sekar, R.P. Ramasamy, Electrochemical impedance spectroscopy for microbial fuel cell characterization, J. Microb. Biochem. Technol. S 6 (2013).

[19] K.R. Cooper, M. Smith, Electrical test methods for on-line fuel cell ohmic resistance measurement, J. Power Sources 160 (2006) 1088–1095.

[20] X.-Z.R. Yuan, C. Song, H. Wang, J. Zhang, Electrochemical Impedance Spectroscopy in PEM Fuel Cells: Fundamentals and Applications, Springer Science & Business Media, 2009.

[21] R. Zhao, P.M. Biesheuvel, H. Miedema, H. Bruning, A. Van der Wal, Charge efficiency: a functional tool to probe the double-layer structure inside of porous electrodes and application in the modeling of capacitive deionization, J. Phys. Chem.

Lett. 1 (2009) 205–210.
[22] E. Avraham, M. Noked, Y. Bouhadana, A. Soffer, D. Aurbach, Limitations of charge efficiency in capacitive deionization processes III: the behavior of surface oxidized activated carbon electrodes, Electrochim. Acta 56 (2010) 441–447.
[23] S.A. Hawks, A. Ramachandran, S. Porada, P.G. Campbell, M.E. Suss, P.M. Biesheuvel, J.G. Santiago, M. Stadermann, Performance metrics for the objective assessment of capacitive deionization systems, Water Res. 152 (2019) 126–137.
[24] J.E. Dykstra, S. Porada, A. van der Wal, P.M. Biesheuvel, Energy consumption in capacitive deionization–constant current versus constant voltage operation, Water Res. 143 (2018) 367–375.
[25] R. Zhao, S. Porada, P.M. Biesheuvel, A. Van der Wal, Energy consumption in membrane capacitive deionization for different water recoveries and flow rates, and comparison with reverse osmosis, Desalination 330 (2013) 35–41.
[26] L. Agartan, B. Akuzum, T. Mathis, K. Ergenekon, E. Agar, E.C. Kumbur, Influence of thermal treatment conditions on capacitive deionization performance and charge efficiency of carbon electrodes, Sep. Purif. Technol. 202 (2018) 67–75.
[27] L. Wang, S. Lin, Intrinsic tradeoff between kinetic and energetic efficiencies in membrane capacitive deionization, Water Res. 129 (2018) 394–401.
[28] K. Zuo, J. Kim, A. Jain, T. Wang, R. Verduzco, M. Long, Q. Li, Novel composite electrodes for selective removal of sulfate by the capacitive deionization process, Environ. Sci. Technol. 52 (2018) 9486–9494.
[29] I. Cohen, E. Avraham, M. Noked, A. Soffer, D. Aurbach, Enhanced charge efficiency in capacitive deionization achieved by surface-treated electrodes and by means of a third electrode, J. Phys. Chem. C 115 (2011) 19856–19863.
[30] A. Ramachandran, D.I. Oyarzun, S.A. Hawks, M. Stadermann, J.G. Santiago, High water recovery and improved thermodynamic efficiency for capacitive deionization using variable flowrate operation, Water Res. 155 (2019) 76–85.
[31] S.A. Hawks, J.M. Knipe, P.G. Campbell, C.K. Loeb, M.A. Hubert, J.G. Santiago, M. Stadermann, Quantifying the flow efficiency in constant-current capacitive deionization, Water Res. 129 (2018) 327–336.
[32] A. Hemmatifar, M. Stadermann, J.G. Santiago, Two-dimensional porous electrode model for capacitive deionization, J. Phys. Chem. C 119 (2015) 24681–24694.
[33] A. Ramachandran, S.A. Hawks, M. Stadermann, J.G. Santiago, Frequency analysis and resonant operation for efficient capacitive deionization, Water Res. 144 (2018) 581–591.
[34] W. Cai, J. Yan, T. Hussin, J. Liu, Nafion-AC-based asymmetric capacitive deionization, Electrochim. Acta 225 (2017) 407–415.
[35] A. Omosebi, X. Gao, J. Landon, K. Liu, Asymmetric electrode configuration for enhanced membrane capacitive deionization, ACS Appl. Mater. Interfaces 6 (2014) 12640–12649.
[36] Y. Liu, C. Nie, L. Pan, X. Xu, Z. Sun, D.H. Chua, Carbon aerogels electrode with reduced graphene oxide additive for capacitive deionization with enhanced performance, Inorg. Chem. Front. 1 (2014) 249–255.
[37] D. He, C.E. Wong, W. Tang, P. Kovalsky, T.D. Waite, Faradaic reactions in water desalination by batch-mode capacitive deionization, Environ. Sci. Technol. Lett. 3 (2016) 222–226.
[38] M.E. Suss, S. Porada, X. Sun, P.M. Biesheuvel, J. Yoon, V. Presser, Water desalination via capacitive deionization: what is it and what can we expect from it? Energy Environ. Sci. 8 (2015) 2296–2319.
[39] C. Zhang, D. He, J. Ma, W. Tang, T.D. Waite, Faradaic reactions in capacitive deionization (CDI)-problems and possibilities: a review, Water Res. 128 (2018) 314–330.
[40] W. Tang, D. He, C. Zhang, P. Kovalsky, T.D. Waite, Comparison of Faradaic reactions in capacitive deionization (CDI) and membrane capacitive deionization (MCDI) water treatment processes, Water Res. 120 (2017) 229–237.
[41] O.M. Owoseni, Evaluation of Brackish Water Desalination by Membrane Capacitive Deionization Systems: Performance Tradeoffs in Salt Removal, Hydraulic Recovery, Charge Efficiency, and Specific Energy Consumption, The University of Texas at El Paso, 2018.
[42] Y. Qu, T.F. Baumann, J.G. Santiago, M. Stadermann, Characterization of resistances of a capacitive deionization system, Environ. Sci. Technol. 49 (2015) 9699–9706.
[43] J.C. Farmer, D.V. Fix, G.V. Mack, R.W. Pekala, J.F. Poco, Capacitive deionization of NaCl and NaNO3 solutions with carbon aerogel electrodes, J. Electrochem. Soc. 143 (1996) 159–169.
[44] X. Wang, M. Li, Y. Chen, R. Cheng, S. Huang, L. Pan, Z. Sun, Electrosorption of NaCl solutions with carbon nanotubes and nanofibers composite film electrodes, Electrochem. Solid-State Lett. 9 (2006) E23–E26.
[45] Y.-J. Kim, J.-H. Choi, Enhanced desalination efficiency in capacitive deionization with an ion-selective membrane, Sep. Purif. Technol. 71 (2010) 70–75.
[46] S. Porada, L. Weinstein, R. Dash, A. Van Der Wal, M. Bryjak, Y. Gogotsi, P.M. Biesheuvel, Water desalination using capacitive deionization with microporous carbon electrodes, ACS Appl. Mater. Interfaces 4 (2012) 1194–1199.
[47] M. Suss, Capacitive Water Desalination with Hierarchical Porous Electrodes, Stanford University, 2013.
[48] E. García-Quismondo, R. Gómez, F. Vaquero, A.L. Cudero, J. Palma, M. Anderson, New testing procedures of a capacitive deionization reactor, Phys. Chem. Chem. Phys. 15 (2013) 7648–7656.
[49] R. Zhao, P.M. Biesheuvel, A. Van der Wal, Energy consumption and constant current operation in membrane capacitive deionization, Energy Environ. Sci. 5 (2012) 9520–9527.
[50] L. Wang, S. Lin, Membrane capacitive deionization with constant current vs constant voltage charging: which is better? Environ. Sci. Technol. 52 (2018) 4051–4060.
[51] J.-H. Choi, Comparison of constant voltage (CV) and constant current (CC) operation in the membrane capacitive deionisation process, Desalin. Water Treat. 56 (2015) 921–928.
[52] E. García-Quismondo, C. Santos, J. Soria, J.S. Palma, M.A. Anderson, New operational modes to increase energy efficiency in capacitive deionization systems, Environ. Sci. Technol. 50 (2016) 6053–6060.
[53] W. Tang, D. He, C. Zhang, T.D. Waite, Optimization of sulfate removal from brackish water by membrane capacitive deionization (MCDI), Water Res. 121 (2017) 302–310.
[54] Y. Jande, W. Kim, Desalination using capacitive deionization at constant current, Desalination 329 (2013) 29–34.
[55] J. Kang, T. Kim, H. Shin, J. Lee, J. Ha, J. Yoon, Direct energy recovery system for membrane capacitive deionization, Desalination 398 (2016) 144–150.
[56] L. Wang, J. Dykstra, S. Lin, Energy efficiency of capacitive deionization, Environ. Sci. Technol. 53 (2019) 3366–3378.
[57] F. He, P.M. Biesheuvel, M.Z. Bazant, T.A. Hatton, Theory of water treatment by capacitive deionization with redox active porous electrodes, Water Res. 132 (2018) 282–291.
[58] P.M. Biesheuvel, R. Zhao, S. Porada, A. Van der Wal, Theory of membrane capacitive deionization including the effect of the electrode pore space, J. Colloid Interface Sci. 360 (2011) 239–248.
[59] P.M. Biesheuvel, Y. Fu, M.Z. Bazant, Diffuse charge and Faradaic reactions in porous electrodes, Phys. Rev. E 83 (2011) 061507.
[60] W. Tang, P. Kovalsky, B. Cao, D. He, T.D. Waite, Fluoride removal from brackish groundwaters by constant current capacitive deionization (CDI), Environ. Sci. Technol. 50 (2016) 10570–10579.
[61] R. Zhao, O. Satpradit, H. Rijnaarts, P.M. Biesheuvel, A. Van der Wal, Optimization of salt adsorption rate in membrane capacitive deionization, Water Res. 47 (2013) 1941–1952.